Astronomy & Astrophysics manuscript no. GC_starcounts_Gallego
January 17, 2017
©ESO 2017

The distribution of old stars around the Milky Way's central black hole: I. Star counts

E. Gallego-Cano[1], R. Schödel[1], H. Dong[1], F. Nogueras-Lara[1], A. T. Gallego-Calvente[1], P. Amaro-Seoane[2], and H. Baumgardt[3]

[1] Instituto de Astrofísica de Andalucía (CSIC), Glorieta de la Astronomía s/n, 18008 Granada, Spain e-mail: lgc@iaa.es
[2] Institut de Ciències de l'Espai (CSIC-IEEC) at Campus UAB, Carrer de Can Magrans s/n 08193 Barcelona, Spain
Institute of Applied Mathematics, Academy of Mathematics and Systems Science, Chinese Academy of Sciences, Beijing 100190, China
Kavli Institute for Astronomy and Astrophysics, Beijing 100871, China
Zentrum für Astronomie und Astrophysik, TU Berlin, Hardenbergstraße 36, 10623 Berlin, Germany
[3] School of Mathematics and Physics, University of Queensland St. Lucia, QLD 4068,Australia

Received; accepted

arXiv:1701.03816v1 [astro-ph.GA] 13 Jan 2017

ABSTRACT

Context. The existence of dynamically relaxed stellar density cusps in dense clusters around massive black holes is a long-standing prediction of stellar dynamics, but it has so far escaped unambiguous observational confirmation.
Aims. In this paper we revisit the problem of inferring the innermost structure of the Milky Way's nuclear star cluster via star counts, to clarify whether it displays a core or a cusp around the central black hole.
Methods. We use judiciously selected adaptive optics assisted high angular resolution images obtained with the NACO instrument at the ESO VLT. Through image stacking and improved PSF fitting we push the completeness limit about one magnitude deeper than in previous, comparable work. Crowding and extinction corrections are derived and applied to the surface density estimates. Known young, and therefore dynamically not relaxed stars, are excluded from the analysis. Contrary to previous work, we analyse the stellar density in well-defined magnitude ranges in order to be able to constrain stellar masses and ages.
Results. We focus on stars in the Red Clump (RC), with observed magnitudes $K \approx 15.5$, and on stars with observed magnitudes $K \approx 18$, which we expect to have similar mean ages and masses than the former. The RC and brighter giant stars display a core-like surface density profile within a projected radius $R < 0.3$ pc of the central black hole, in agreement with previous studies, but show a cusp-like surface density distribution at larger R. The surface density of the fainter stars can be described well by a single power-law at $R < 2$ pc. The cusp-like profile of the faint stars persists even if we take into account the possible contamination of stars in this brightness range by young pre-main sequence stars. The data are inconsistent with a core-profile for the faint stars. We exclude from our analysis the region $R < 1''/0.04$ pc, where the density is less than expected at all brightness ranges, because this region may be too crowded and also has suffered changes to its stellar population beyond dynamical relaxation. Finally, we show that a 3D *Nuker* law provides a very good description of the cluster structure.
Conclusions. We conclude that the observed stellar density at the Galactic Centre, as it can be inferred with current instruments, is consistent with the existence of a stellar cusp around the Milky Way's central black hole, Sagittarius A*. This cusp is well developed inside the influence radius of about 3 pc of Sagittarius A* and can be described by a single three-dimensional power-law with an exponent $\gamma = 1.23 \pm 0.05$. This corroborates existing conclusions from Nbody simulations performed in a companion paper. The apparent lack of RC stars and brighter giants at projected distances of $R \lesssim 0.3\,pc$ ($R \lesssim 8''$) of the massive black hole may indicate that some mechanism has altered their distribution or intrinsic luminosity. We estimate the number of possibly missing giants to a few dozen. This value agrees well with the theoretical idea that a previously existing gaseous fragmenting disc around Sagittarius A*, precursor of the observed young, massive stars, was responsible for rendering giant stars invisible.

Key words. Galaxy: center – Galaxy: kinematics and dynamics – Galaxy: nucleus

1. Introduction

This is the first one of three papers addressing the distribution of stars around Sagittarius A* (Sgr A*), the massive black hole at the centre of the Milky Way. They are closely related, but focus on different methods and stellar populations. In this work we use the method of star counts, while in our other paper (Schödel et al., referred to as Paper II in the following), we analyse the diffuse light from the unresolved stellar population. Finally, Baumgardt et al. (Paper III) present new Nbody simulations that confirm the agreement between modelling and observations.

The distribution of stars around Sgr A* is of great astrophysical interest because it is the only massive black hole where we can test observationally the existence of a stellar cusp. Such a stellar cusp is a prediction of stellar dynamics for the case of a dynamically relaxed cluster and has been derived and studied by analytical, Monte Carlo and N-body methods (e.g., Bahcall & Wolf 1976; Lightman & Shapiro 1977; Murphy et al. 1991; Baumgardt et al. 2004; Amaro-Seoane et al. 2004; Alexander & Hopman 2009; Preto & Amaro-Seoane 2010). These consistent theoretical results have, however, not yet been confirmed observationally. There exist currently only measurements of about two dozen systems, where we can actually resolve the radius of influence of the central black hole with several resolution elements (see, e.g., Table 1 in Gültekin et al. 2009). The great dis-

tance of most extragalactic systems means that we can only study the light density of hundreds to thousands, or even millions, of stars per resolution element. Since nuclear star clusters are entities with complex stellar populations, many of which show signs of recent star formation (see review by Böker 2010), measured light densities may frequently be dominated by a small number of bright stars, which are generally too young to be dynamically relaxed. This can lead to ambiguous or erroneous results.

On the other hand, with its distance of only about 8 kpc from Earth, the Galactic Centre (GC) allows us to resolve the stars observationally on scales of about 2 milli-parsecs (mpc), assuming diffraction limited observations at about 2 μm at an 8-10m telescope. At the centre of the Milky Way, a 4×10^6 $M_\odot$ (e.g., Boehle et al. 2016; Gillessen et al. 2016) massive black hole, Sagittarius A* (Sgr A*), lies embedded in a $\sim2.5\times10^7$ $M_\odot$ nuclear star cluster (Schödel et al. 2014a,b). Therefore, the GC appears to be, in principle, the ideal test case for the existence of stellar cusps.

Surprisingly, no unambiguous observational evidence for the existence (or not) of a stellar cusp around Sgr A* has been presented so far. While the first high angular resolution observations at an 8m telescope appeared to indicate the existence of a stellar cusp (Genzel et al. 2003; Schödel et al. 2007), it was later realised that the star counts within about 0.5 pc of Sgr A* were contaminated by a significant number of young, and therefore dynamically unrelaxed, stars. When omitting the young stars, the projected stellar density of giants appears almost flat, core-like, within a few 0.1 pc of Sgr A* (Buchholz et al. 2009; Do et al. 2009; Bartko et al. 2010). Observations of the stellar surface brightness from old stars also appeared to indicate a possibly core-like structure (Fritz et al. 2016). These findings led to the *missing cusp problem* and have given rise to a large number of theoretical papers, trying to explain its absence. The hypotheses reach from a very long relaxation time (Merritt 2010), over the destruction of the envelopes of giants – thus rendering them invisible – via stellar collisions, which cannot fully explain the observations (Dale et al. 2009) or a fragmented gaseous disc, which can (Amaro-Seoane & Chen 2014). Other explanations involve the apparent stellar structure arising from subsequent epochs of star formation and/or the accumulation of stellar remnants near Sgr A* (e.g., Löckmann et al. 2010; Aharon & Perets 2015).

When evaluating the observational evidence, it is, however, of utmost importance to be aware of its limitations. Firstly, due to the extreme interstellar extinction toward the Galactic Centre (e.g., Nishiyama et al. 2009; Schödel et al. 2010; Fritz et al. 2011), observations need to be performed in the near-infrared (NIR). A second requirement for observing the Galactic Centre (GC) is to use an angular resolution as high as possible to overcome the extreme source crowding. Here we use the adaptive optics (AO) assisted NIR camera NACO installed at the ESO VLT. Imaging data at H and K_S are used to be able to estimate extinction and – by the same means – to exclude foreground stars.

Because of these observational difficulties, our knowledge about the stellar population at the GC is limited to the brightest few percent of stars: A few million-year-old hot post main sequence (MS) giants and MS O/B stars (the latter being already at the faint limit of spectroscopic capabilities), on the one hand, and, on the other hand, giants with luminosities equal to or higher than RC stars. In fact, the typical spectroscopic completeness reaches only about $K_S = 15.5$ stars and thus only half the RC (see Do et al. 2009; Bartko et al. 2010; Do et al. 2015). Studies of the stellar surface density at the GC have so far been dominated by RC stars and brighter giants. The only recent study that focused on the light from stars fainter than this limit did indeed find a cusp-like structure within 5"/0.2 pc of Sgr A* (Yusef-Zadeh et al. 2012). Hence, we have only observed the tip of the iceberg, which may not be representative for the overall, underlying structure.

This work continues similar efforts carried out by Genzel et al. (2003) and Schödel et al. (2007). As experiments are repeated, both their accuracy and precision tend to increase because of factors such as improvements in observational techniques, increasing know-how on data reduction and analysis, progress in theory and interpretation, and an increasing amount of data. The novel aspects of this work are, in particular, the stacking of high quality images with a large field-of-view (FOV) to reach fainter completeness limits in the most crowded regions near Sgr A*, an extension of high angular resolution data to a larger field of about $1.5' \times 1.5'$, improvements in data reduction (rebinning of the images, removal of systematic noise from detector electronics), and analysis (improved PSF fitting with use of noise maps and a spatially variable PSF). Finally, more explicitly than in previous work – and because our deeper data allow us to do so – we focus on clearly delimited stellar brightness ranges in order to minimise the mixing of different stellar populations. We add new data on the stellar distribution at projected radii $R \gtrsim 2$ pc from the literature (Schödel et al. 2014a; Fritz et al. 2016) to facilitate the interpretation of the data and the derivation of the 3D density structure of the stars near the massive black hole.

2. Data reduction and analysis

2.1. Basic reduction

We use H and Ks-band data obtained with the S27 camera (0.027" pixel scale) of NACO/VLT. The AO was locked on the NIR bright supergiant GCIRS 7 that is located about 5.5" north of Sgr A*. The data used are summarised in Table 1. All data were acquired with a similar 4 point dither pattern, roughly centered on Sgr A*, with the exception of the data from 11 May 2011, which covered a shallow, but wider mosaic with a 4×4 dither pattern, centered on Sgr A*. Preliminary data reduction was standard, with sky subtraction, bad pixel removal and flat fielding. Subsequently, a simple shift-and-add (SSA) procedure was applied to obtain final images. A quadratic interpolation with a rebinning factor of two was used because tests showed that this improved the photometry and reduced residuals in PSF fitting, in particular since the S27 pixel scale barely samples the angular resolution, which was roughly 0.06" FWHM for all images. Along with the mean SSA images we also created noise maps that contain the error of the mean of each pixel in the SSA images.

2.2. Alignment and stacking

We treated each of the four pointings toward Sgr A* independently to avoid problems arising from camera distortions near the edges of the NACO S27 camera's field (see Trippe et al. 2008; Schödel et al. 2009). The final images from all epochs were aligned with the one from 09 Aug 2012 via a polynomial fit of degree one (IDL POLYWARP and POLY_2D procedures). The parameters of the latter were determined via an iterative fit using lists of detected stars in the image. The images were combined in a simple mean and the corresponding noise maps were quadratically combined. A possible concern in this stacking procedure is the use of different observing epochs because of the large proper motions of the stars in the GC. At the distance of the GC (here assumed as 8 kpc, see, e.g., Genzel et al. 2010; Meyer

Table 1. Details of the imaging observations used in this work.

Date[a]	$\lambda_{central}$ [μm]	$\Delta\lambda$ [μm]	N[b]	NDIT[c]	DIT[d] [s]
09 May 2010	1.66	0.33	4	64	2
17 May 2011	2.18	0.35	4	9	2
09 Aug 2012	2.18	0.35	8	60	1
11 Sep 2012	2.18	0.35	8	60	1
12 Sep 2012	2.18	0.35	8	60	1

[a] UTC date of beginning of night.

[b] Number of (dithered) exposures

[c] Number of integrations that were averaged on-line by the read-out electronics

[d] Detector integration time. The total integration time of each observation amounts to N×NDIT×DIT.

et al. 2012), a velocity of about 40 km s^{-1} on the plane of the sky corresponds to a proper motion of one milli-arcsecond per year. A displacement by one pixel of the NACO S27 camera per year therefore corresponds to a velocity > 1000 km s^{-1}. Since we are not interested in high precision astrometry or photometry, this effect is therefore negligible for our data, except possibly a small number of very fast moving stars within ~0.1" of Sgr A*, which is not relevant to the problem and scales addressed in this paper.

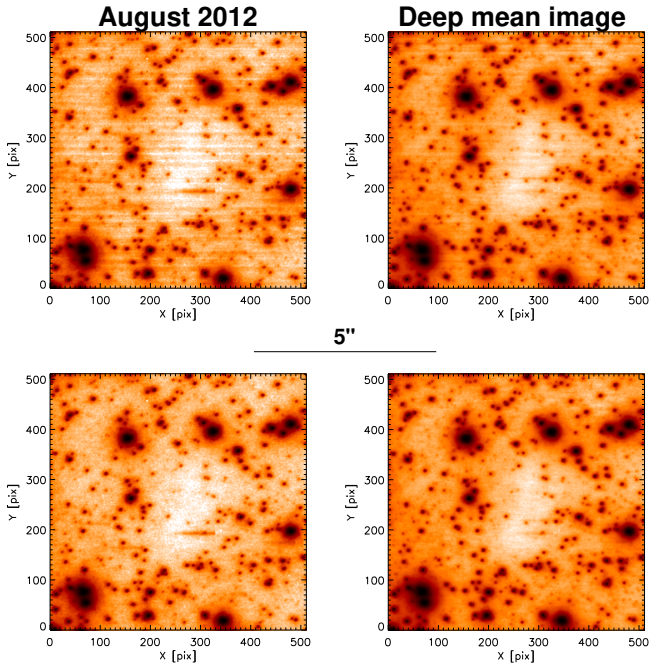

Fig. 1. Cleaning of horizontal stripes (systematic readout noise). Upper left: Detail of August 2012 Ks-band image. Lower left: As upper left, but cleaned. Upper right: Detail of deep, mean combined Ks-band image when the input images have not been cleaned. Lower right: Detail of deep, mean combined Ks-band image after cleaning of the input images. The displayed field is located about 12.0" west and 1.7" north of Sgr A*. The colour scale is logarithmic and identical for all images.

2.3. Pattern removal

The images from the individual epochs contained horizontal stripe patterns from the detector electronics. These horizontal stripes can be detrimental for source detection because they may either mask faint sources or be deblended into rows of stars by the PSF fitting program. It is therefore important to remove them. We proceeded as follows: We used the *StarFinder* program to detect and subtract robustly detected point sources from each image (conservative settings of the *StarFinder* parameters: *min_correlation*= 0.85 and *deblend*= 0) and to fit the diffuse emission (from unresolved stars or dust and gas in the interstellar medium). The latter was fitted with an angular resolution of about 0.25", a non-critical value that just needs to be large enough to remove the variable background due to unresolved stellar emission and small enough to roughly correspond to the size of diffuse, uncresolved structures in the mini-spiral (see Paper II). While fitting of the diffuse background is important in this procedure, the exact choice of its variability scale is not. It can easily be chosen to be a factor 2 larger or smaller.

The resulting residual images, i.e. image minus diffuse emission minus point sources, were then dominated by small-scale (on the order a few pixels width) random and systematic noise. We determined the pattern of horizontal stripes induced by the electronics through median smoothing each row of pixels with a median box width of about 2.7", corresponding to 200 pixels (in the rebinned images). This pattern was then subtracted from the SSA images. We could thus remove most of the systematic noise without introducing any significant bias on the point sources or on the diffuse emission because most stars had already been subtracted and because the median smoothing box was a factor of a few to ten larger than the scales of the diffuse emission, of the size of PSF residuals, or of faint, unresolved sources. Finally, after having cleaned the images of each epoch, they were combined to a deep mean image. This last step further reduced any remaining systematics. To be conservative, we used the noise maps derived from the uncleaned images. Figure 1 shows details of K_s-images to illustrate the effect of the systematic readout noise and the improvement after removing it.

2.4. Source detection

Point source extraction was carried out with the PSF fitting programme *StarFinder* (Diolaiti et al. 2000). Since the images cover areas similar to or larger than the isoplanatic angles at the respective wavelengths, care was taken to deal with the spatial variability of the PSF. We parted the images into sub-fields of approximately 10.5" × 10.5" size. Subsequently, ten of the brightest, most isolated stars in each sub-field were used for an iterative extraction of a local PSF (similar to what was done in Schödel et al. 2010). Because of variable extinction and source density, not all sub-fields contained PSF reference stars of similar brightness, which would lead to a systematic change of the zero point across the field. Also, not taking into account the extended seeing halo from the light that could not be corrected by the AO, can lead to an enhanced detection of spurious faint stars near bright stars. As remarked by Schödel (2010), the seeing halo is affected in a rather minor way by anisoplanatic effects. We therefore used the brightest star in the field, GCIRS 7, to estimate the seeing halo. The local PSFs were masked beyond radii of about 0.3", up to which they could be reliably determined. Then they were matched to the seeing halo (using a least-squares fit to determine flux offsets and normalisation factors). Thus, we could create local PSFs that avoided large systematic photometric effects across

the field. Some tests (similar to what was done in Schödel 2010) showed that we could constrain the systematic photometric effects from the variability of the PSF to a few percent across the field.

In PSF fitting we have to walk a thin line between achieving an almost complete detection of sources while, at the same time, avoiding to pick up spurious ones, which can arise, in particular, close to bright stars or due to systematic effects from the detector electronics. We visually verified that taking the PSF seeing halos into account, along with the use of our SSA noise maps, effectively suppressed the detection of spurious sources near bright stars (see also Schödel et al. 2013). The PSF halos include effects such as diffraction spikes and static speckles. Our empirical noise maps seemed to deal well with suppressing the detection of spurious sources near bright stars.

Finally, since there can be no absolute certainty in the reliability of source detection, we also repeatedly analysed the images with different values of the *StarFinder* parameters that dominate the probability of source detection (for a fixed detection threshold, which was chosen as 3σ in all cases). These parameters are *min_correlation* and *deblend*. For the minimum correlation value we chose $0.8 - 0.9$, always more conservative than the standard value of 0.7, the default value of *StarFinder*. The key word *deblend* can be set to deblend close sources. While deblending can be very useful, it can lead also to the detection of a significant number of spurious sources in a crowded field. We included measurements with and without setting this keyword.

2.5. Photometric calibration and source selection

Finally, the photometry was calibrated with the stars IRS 16C, IRS 16NW, and IRS 33N (apparent magnitudes $K_s = 9.93, 10.14, 11.20$ and $H = 11.90, 12.03, 13.24$, see Schödel et al. 2010). The uncertainty of the zero points was a few percent. We note that for the purposes in this paper we do not require any high accuracy/high precision photometry and astrometry.

Almost all stars in the field have intrinsic colours $-0.1 \leq H - K \leq 0.3$ (see, e.g., Do et al. 2009; Schödel et al. 2010). The mean colour due to reddening is $H - K \approx 2.1$. We excluded all stars with $H - K < 1.5$ as foreground stars. We also excluded spectroscopically identified young stars from our final star list (Do et al. 2009; Bartko et al. 2010). Subsequently, we created an extinction map, by using the 20 stars nearest to each point. The resulting map is similar, to within the uncertainties, to the one presented in Schödel et al. (2010).

2.6. Crowding and completeness

We determined the source detection completeness in the K_s-images through the technique of inserting and recovering artificial stars. We used a magnitude step of 0.5 mag and inserted the stars on a 0.5" × 0.5" grid. With this relatively wide spacing we avoided artificially increasing the crowding. The grid was shifted several times to finally probe completeness on a dense 0.1"×0.1" grid (as done by Schödel et al. 2007). We used the respective local PSFs (see above). Subsequently, PSF fitting was carried out with *StarFinder* and a source was considered as detected if it was found within a magnitude range of 0.5 mag of the input magnitude and within a distance of 0.054" of the input position (corresponding to 2 pixels of the S27 camera or roughly the angular resolution of the data). If a real star of a similar magnitude was already present within this distance to the grid point of an artificial star, then the artificial star was considered as detected. This latter point is critical to avoid bias because the relatively high density of artifically introduced stars would otherwise lead to non-detection of real sources and thus an over-estimation of incompleteness.

As mentioned above, to estimate the systematic errors induced by either the non-detection of real sources or the detection of spurious sources, we repeated the source detection and completeness determination for the following combinations of the *StarFinder* parameters: *min_correlation*= $0.80, 0.85, 0.85, 0.90$ and *deblend*= $0, 0, 1, 1$ (each value in the first list corresponds to the value with the same index in the second list). In Fig. 2, we show the values of completeness for two of these cases and for different projected distance ranges from Sgr A*. The differences between the different choices of parameters are generally small, on the order of a few percentage points, except for the faintest magnitudes, where the differences are somewhat more pronounced. Also, we can observe the expected general trend of less completeness for fainter magnitudes and in the more crowded areas near Sgr A*. Finally, Fig. 2 also shows that the differences of completeness between the four pointings are small. For all cases, we found that source detection was, at all projected distances, at least 50% complete for magnitudes $K_s \leq 18.5$.

2.7. Extinction

We used the $H - K_s$ photometry and the intrinsic small colours of stars at these bands to create an extinction map for the entire field, with the same method as applied in Schödel et al. (2010). We do not consider stars with $H - K_s < 1.5$ because we consider them as foreground stars. Neither do we consider stars with $H - K_s > 3.0$ because they may either be background stars or intrinsically reddened objects (in any case, their number is very small, see Fig 4 in Schödel et al. 2010). Median stellar colours were obtained from the individual colours of the 20 nearest stars at each position and the extinction was then calculated as in Schödel et al. (2010), assuming $A_{K_s} \propto \lambda^{-2.2}$.

On the one hand, the extinction map was used to correct the individual stellar magnitudes for differential extinction. On the other hand, we applied the methodology of Chatzopoulos et al. (2015b) to compute the stellar detection completeness variation caused by variable extinction: We modeled the luminosity function (LF) by taking the product of a power-law stellar LF and an error function that represents the completeness function, as in expression (2) in Chatzopoulos et al. (2015b). The approximation of the LF with a power-law – which ignores the presence of the RC bump – does not introduce any significant error because our data are sensitive enough to reach well below the RC bump over the entire field and because including the RC bump would only have a minor effect as shown by Chatzopoulos et al. (2015b). First, we measured the observed KLF for each pointing and each StarFinder parameter set (excluding a radius of about 5" around Sgr A*, where the KLF is more incomplete because of crowding). We computed the power law for each case. Finally, we used these power-laws, combined it with the measured local extinction and computed the corresponding local correction factors according to equation (5) in Chatzopoulos et al. (2015b), but using the approximation of a single extinction screen, i.e. no variability of A_{K_s} along the line-of-sight. Since we approximate the LF with a power law, the equation takes on the form $p = L(-\Delta A_k) = 10^{-\gamma * \Delta A_k}$ (see Chatzopoulos et al. 2015b), where p is the reduction factor for the number of locally detected stars, ΔA_k is the difference between the local extinction and the mean

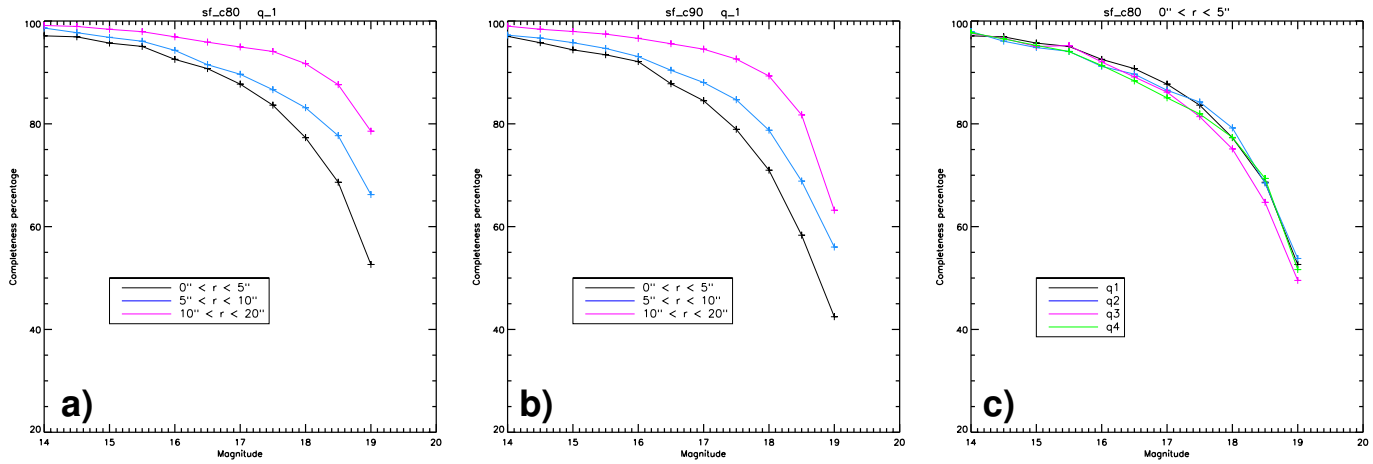

Fig. 2. Completeness of the star counts in the deep NACO K_s images. a) Completeness in pointing 1 for different projected distance ranges from Sgr A*, for *min_correlation*= 0.80 and *deblend*= 0. b) As in a), but for *min_correlation*= 0.90 and *deblend*= 1. c) Completeness for all four pointings and within 5" of Sgr A*, for *min_correlation*= 0.80 and *deblend*= 0. The corresponding plots for other used combinations of *min_correlation and deblend* look very similar.

extinction over the field, and γ is the power law index of the luminosity function. If the local extinction is lower than the mean extinction, then $p > 1$, and if the local extinction is higher than the mean extinction, then $p < 1$.

We apply the correction factor $1/p$ to each detected star. In Fig. 3 we show the K_s LF for pointing 1 , for *min_correlation*= 0.8 and *deblend*= 0, along with the LF corrected for differential extinction, a power law fit to the stars $11 < K_s < 14.5$ ($\gamma = 0.26 \pm 0.02$,similar to the value obtained in Schödel et al. (2010)), and the completeness function (blue line), as defined by Chatzopoulos et al. (2015b). For the latter, we use $m_0 = 19.4$ and $\sigma = 0.2$ because these values approximate our K_s LF well. These values are different from those used in Chatzopoulos et al. (2015b) because our data are significantly deeper than theirs. In Fig. 4 the percentage reduction in observed stars versus projected radius is represented for the detected stars in pointing 1,for *min_correlation*= 0.8 and *deblend*= 0. One can see that extinction is, on average, higher at larger distances from Sgr A*, but that the effect of differential extinction on completeness is relatively minor, typically < 10% and at most 20%.

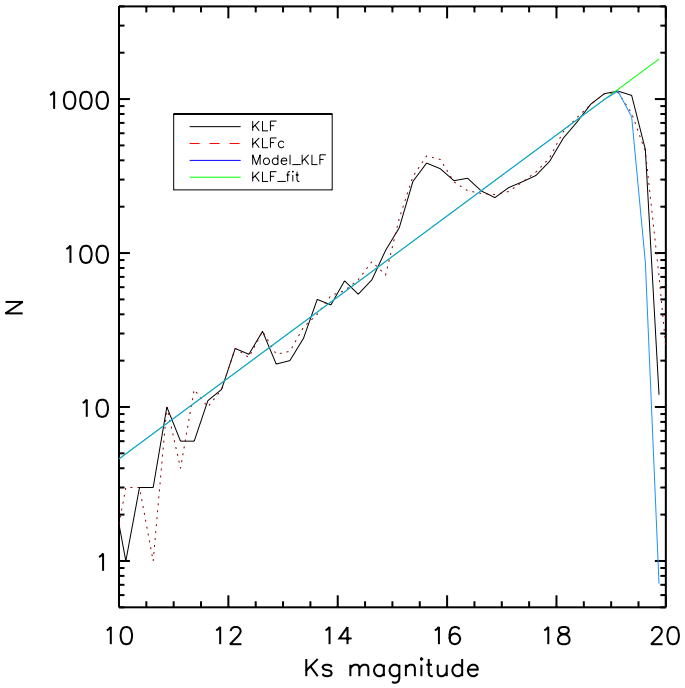

Fig. 3. The Ks LF in pointing 1 for *min_correlation*= 0.8 and *deblend*= 0 if shown as a black line. The dotted red line is the K_s LF after correcting the magnitude of each star for differential extinction. The green lines shows a power law fit to the bright stars $11 < K_s < 14.5$ with power law index of 0.26 ± 0.02. The blue line shows the effect of the completeness function according to equation (2) in Chatzopoulos et al. (2015b).

2.8. Wide field

The 2011 data are of excellent quality, but relatively shallow. On the other hand, there are 16 pointings that cover a field of about $1.5' \times 1.5'$, compared to the smaller fields of about 40"×40" covered by the other NACO observations. The 2011 observations are therefore ideally suited to extend the sensitive central observations with high angular resolution, albeit somewhat shallower, data out to larger distances. Fig. 5. In order to deal with the distortions of the NACO S27 camera (see, e.g., Trippe et al. 2008; Schödel et al. 2009) we aligned each pointing of the NACO mosaic with a reference frame created from positions measured in HST WFC3 observations of the same field (Dong et al., in prep.). We apply variable PSF fitting as we explain in section 2.4. In this case, *min_correlation*= 0.8 and *deblend*= 0 were selected for the *StarFinder* parameters.

3. The surface density of old stars in the GC

3.1. K_s luminosity function

We show the K_s LF (KLF) determined from our deep mosaic in Fig. 6. The KLFs corresponding to the four different *StarFinder* parameter settings are shown. The KLF derived in this work is about one magnitude deeper compared to previous work (Fig. 10 in Schödel et al. 2007). This is a decisive advantage. When we want to probe the existence of a dynamically relaxed stellar cusp around Sgr A*, we need to focus on stars that are at least sev-

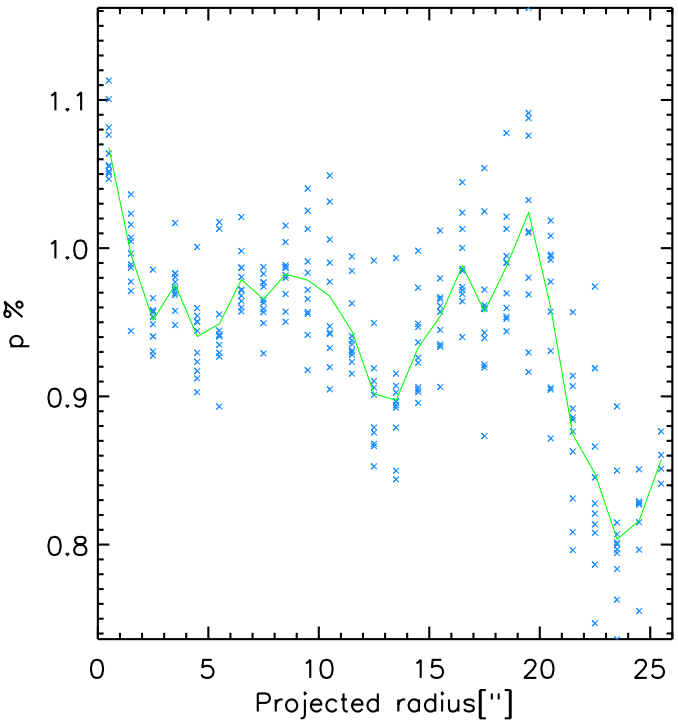

Fig. 4. Relative detection frequency due to extinction versus projected distance to Sgr A*, in pointing 1 for *min_correlation*= 0.8 and *deblend*= 0. The green line represents the mean of the $p(\%)$ considering detected stars at the same distance from Sgr A*. We can observe that for close distances to Sgr A* $p(\%)$ is higher than for large distances, as we expected, because the extinction near Sg A* is lower.

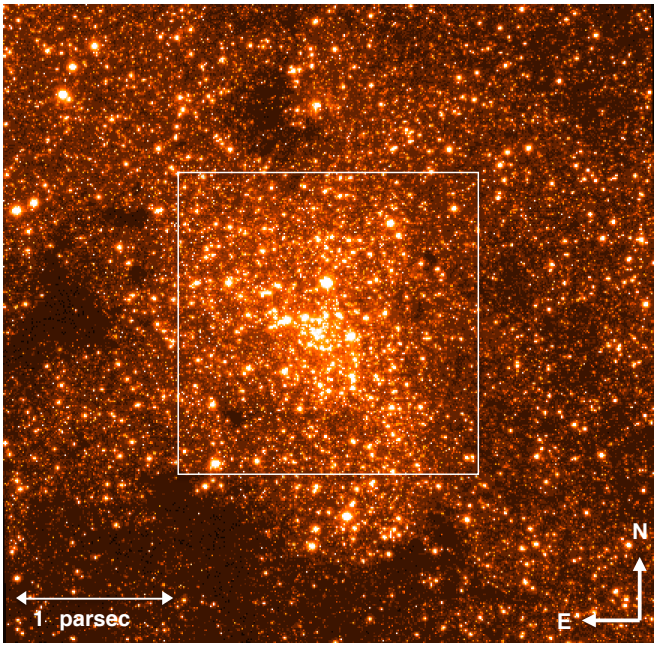

Fig. 5. Wide-field mosaic of the observations from 11th May 2011. The field-of-view is $1.5' \times 1.5'$. The field of about 40"×40" that corresponds to the deep imaging data is marked by a white square.

eral Gyr old. As shown in the illustrative Figure 16 in Schödel et al. (2007), the only magnitude range where this was previously possible was around the RC ($15.25 \leq K_s \leq 16.25$). Now, with the deeper data from our new analysis, we can probe another, fainter magnitude range with a high fraction of old stars ($17.5 \leq K_s \leq 18.5$). Also, the stars in these two brightness ranges have similar masses, which lets us expect a similar surface density distribution.

The goal of this study is to investigate the existence of a stellar cusp at the GC. This requires us to select stars old enough to have undergone dynamical relaxation. The relaxation time at the GC is roughly a few Gyr (e.g., Alexander 2005, 2011). We specifically exclude all spectroscopically identified early-type, i.e. young and massive, stars from our sample (using the data of Do et al. 2013). Unfortunately, spectroscopic stellar classification is limited to stars of about $K_s \leq 15.5$ at the GC. For fainter stars, we can only use their luminosity as a proxy for their type. Fig. 16 of Schödel et al. (2007) illustrates the LF, mean masses, and old star fractions for stars of different magnitudes at the GC, assuming a basic continuous star formation model. It shows that we can probe old ($\gtrsim 1$ Gyr), low-mass stars in the range $15 \lesssim K_s \leq 16$. This is the RC, which dominates all previous star density measurements. The fraction of old stars rises again above ~50% for stars $K_s > 17.5$, reaching practically 100% at $K_s \approx 18$. Therefore, in this study, we focus on the magnitude ranges $15 \leq K_s \leq 16$, the RC, and $17.5 \leq K_s \leq 18.5$, i.e. the faintest stars accessible by our data.

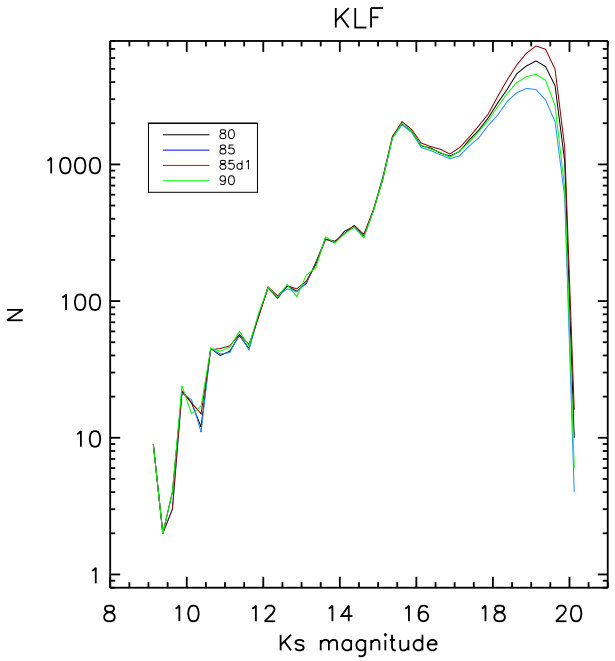

Fig. 6. KLF for the deep K_s mosaic. The different colours correspond to the different combinations of the values of *min_correlation* and *deblend*.

3.2. Radial profile of the number density

In order to analyse the surface density of stars at the Galactic Center, we assume that the underlying spatial distribution of the stars in the central parsec is spherically symmetric. Although the nuclear cluster is flattened, a spherical approximation should be acceptable at projected radii $R \lesssim 2$ pc because the difference between the density profiles along the orthogonal directions of maximum difference is only on the order of 10% – 20% in this region (see Schödel et al. 2014a; Fritz et al. 2016).

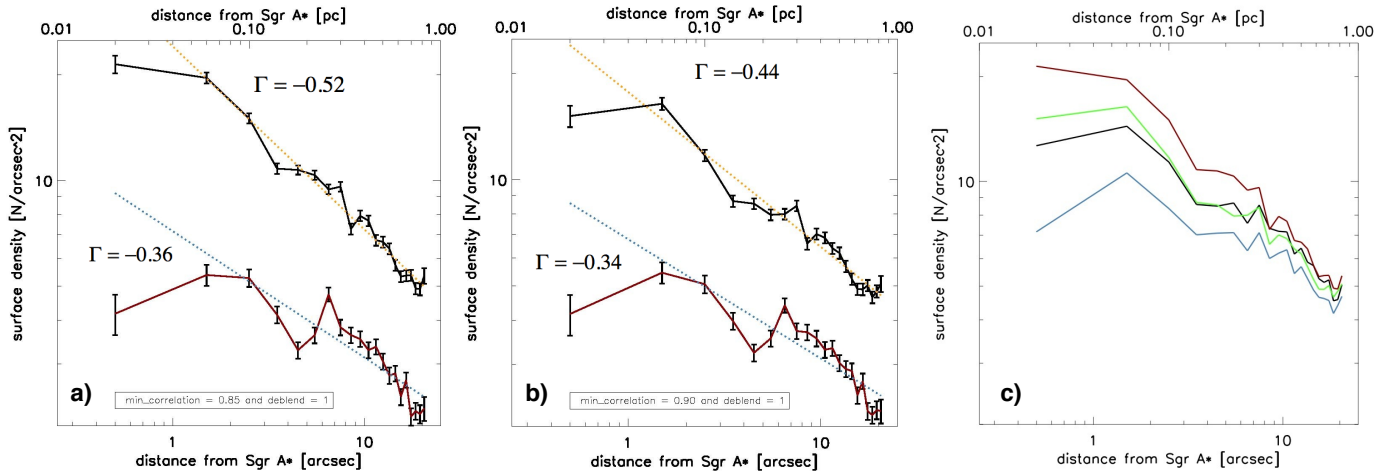

Fig. 8. Azimuthally averaged extinction and crowding corrected surface densities vs. distance from Sgr A*. Straight dotted lines illustrate fits with a single power-law. a) Surface density for *min_correlation*= 0.85 and *deblend*= 1. The value of the power-law index, Γ, for RC stars (red line) is $\Gamma = -0.36 \pm 0.04$ and for fainter stars (black line) is $\Gamma = -0.52 \pm 0.02$. b) Surface density for *min_correlation*= 0.90 and *deblend*= 1. The value of the index for RC stars (red line) is $\Gamma = -0.34 \pm 0.04$ and for fainter stars (black line) is $\Gamma = -0.44 \pm 0.02$. c) Surface density profiles for stars of $17.5 \leq K_s \leq 18.5$ for the data obtained with the different *StarFinder* parameters.

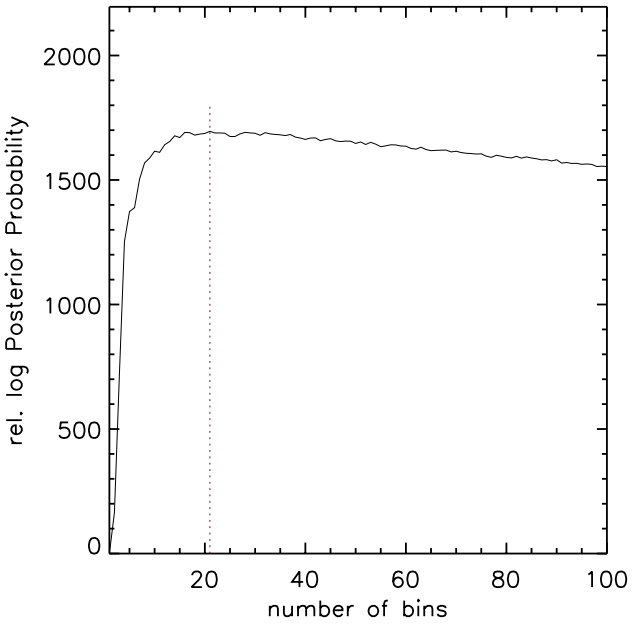

Fig. 7. Optimal binning. We show the RLP as a function of the number of bins. The maximum for the RLP is reached for 21 bins (red dotted line).

We computed the azimuthally averaged stellar surface densities in annuli around Sgr A*. It is important to choose a number of bins sufficiently large to capture the major features in the data while ignoring fine details due to random fluctuations. Following the studies of Knuth (2006) and Witzel et al. (2012) we first determine the best bin size. The dependence of the Relative Logarithmic Posterior Probability (RLP) on the bin number for pointing 1 is shown in Fig. 7. The maximum for the RLP for the star number is reached for 21 bins, and the best bin size is 1″. We applied this methodology for all pointings, with similar results.

We computed extinction and completeness-corrected stellar surface densities for the stars detected in the different *StarFinder* runs. For faint stellar magnitudes, we masked the regions with completeness below 30%. We tested the effect of different masks, with *completeness*< 30%, 40%, 50% respectively, and found that the results did not vary significantly. Fig. 8 shows the radial surface density profiles for RC stars ($K_s \approx 15.5$) and fainter stars ($K_s \approx 18$) for two different combinations of *StarFinder* parameters (left panel: *min_correlation*= 0.85 and *deblend*= 1; middle panel: *min_correlation*= 0.9 and *deblend*= 1). As can be seen, the resulting surface densities are very similar. The right panel of Fig. 8 shows the surface number density profiles for all four difference *StarFinder* parameter settings. Although there are offsets between the densities, their shapes are very similar.

Finally, we combined the surface density profiles obtained with the four settings of the *StarFinder* parameters. Mean densities and standard deviations were computed and all uncertainties were quadratically combined. The resulting final number density profiles for the magnitude ranges $15 \leq K_s \leq 16$ and $17.5 \leq K_s \leq 18.5$ are shown in Fig. 9. Simple power laws were fit to the data at 1" $\leq R \leq$ 20" (0.04 pc $\leq R \leq$ 0.8 pc), i.e. we deliberately left out the innermost data points from the most crowded region around Sgr A*. The corresponding power law indices are $\Gamma_{cusp} = -0.45 \pm 0.03$ for the faint stars and $\Gamma_{cusp} = -0.34 \pm 0.04$ for RC stars. There is a significant dip around $R = 0.2$pc (5″) in the density profile of the RC stars and, possibly, an excess at $R \approx 7$". It can also be seen that a simple power law is a better approximation for the faint stars than for the RC stars.

3.3. Star counts beyond 20"

In order to study the stellar number density in a broader range of distances from Sgr A* we analysed the large mosaic image from the 2011 data. We did not apply any extinction and completeness corrections because the effect of the extinction correction is small and crowding doe not pose any serious problem at $R > 20$" and with the high angular resolution data used here. We did, however mask all the regions occupied by the dark clouds that can be seen show in Fig. 5. Finally, the surface densities from the wide field data were scaled to the completeness and extinc-

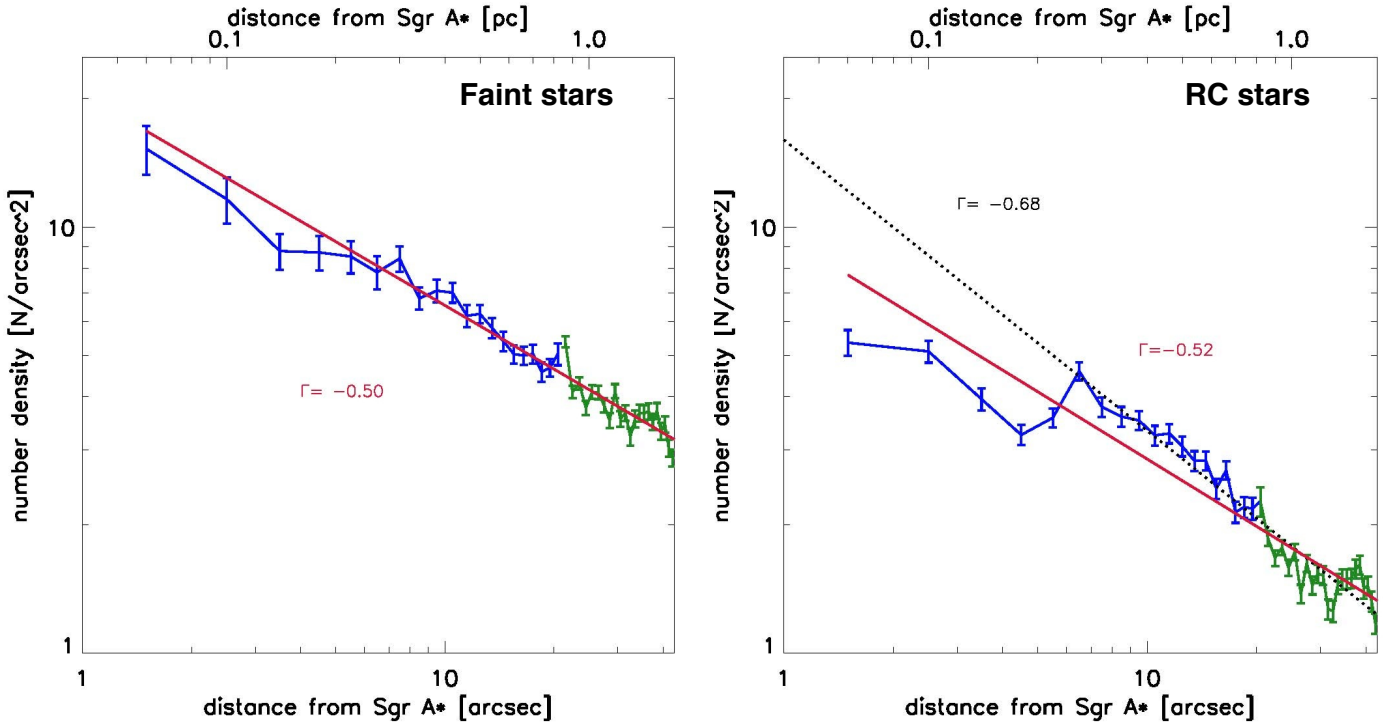

Fig. 10. Combined deep field (blue) plus wide field (green) surface density plots.

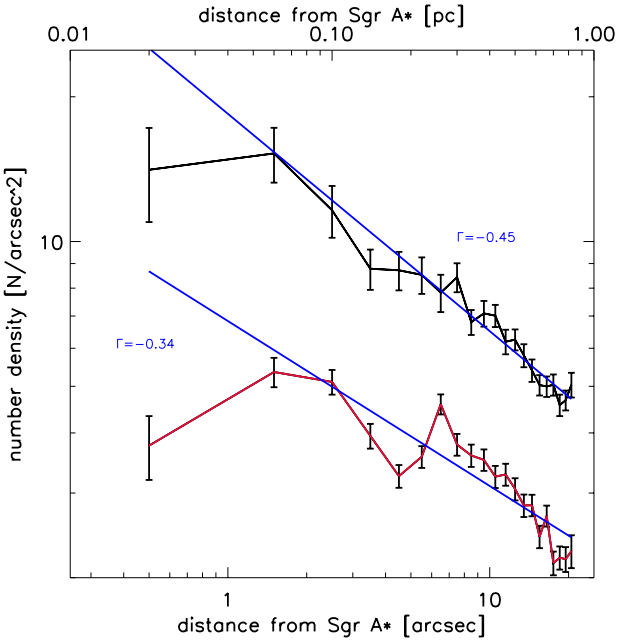

Fig. 9. Azimuthally averaged extinction and crowding corrected surface density vs. distance from Sgr A* for all *StarFinder* data sets and for the K_s-magnitude ranges 15 – 16 (red line) and 17.5 – 18.5 (black line). Blue lines represent simple power-law fits, with the corresponding power-law indices indicated next to the lines.

tion corrected ones from the deep images in the overlap region from $R = 10'' - 20''$. Fig. 10 shows the combined number density plots for stars in the magnitude ranges $16.5 \leq K_s \leq 17.5$ and ($17.5 \leq K_s \leq 18.5$ (left) and RC stars (right), along with simple power-law fits.

3.4. The projected stellar surface density

As Figs. 9 and 10 show, the projected surface number density of the faintest stars in our sample ($17.5 \leq K_s \leq 18.5$) can be described well (reduced $\chi^2 = 2.8$) by a single power-law of the form $\Sigma(R) \propto R^{-\Gamma}$, where Σ is the surface number density, R the projected distance from Sgr A*, and Γ the power-law index. We find $\Gamma = 0.51 \pm 0.02$ for the fit shown in Fig. 10.

The RC stars present a different picture: A single power-law provides only a good fit to the data at $R \gtrsim 6''/0.24$ pc (reduced $\chi^2 = 3.9$), and with a higher value of $\Gamma = 0.68 \pm 0.03$ than in case of the faint stars (see Fig. 10). This value agrees well with what has been found by previous authors for RC and brighter stars (see Schödel et al. 2007, and references therein). Also, the flattening of the RC surface number density inside $R \approx 8''$ agrees very well with previous studies (Buchholz et al. 2009; Do et al. 2009; Bartko et al. 2010). It is interesting to note, however, that $\Gamma = 0.52 \pm 0.03$ if we force a single-power law fit (reduced $\chi^2 = 7.5$) to the RC number density profile, in agreement with the value found for the faint stars.

4. Discussion

4.1. Influence of the correction factors

When determining the number density profile, we have to apply correction factors to compensate the effects of variable stellar crowding and interstellar extinction. Fig. 11 shows the measured surface density profile for stars of magnitude $17.5 \leq K_s \leq 18.5$ without any correction applied (blue), after applying the completeness correction for crowding (red), and after applying the completeness corrections for crowding and extinction (black). As we can see, the completeness correction steepens the profile somewhat. The extinction correction only introduces minor changes because the azimuthal averaging compensates most of the effects of differential extinction across the field. In summary,

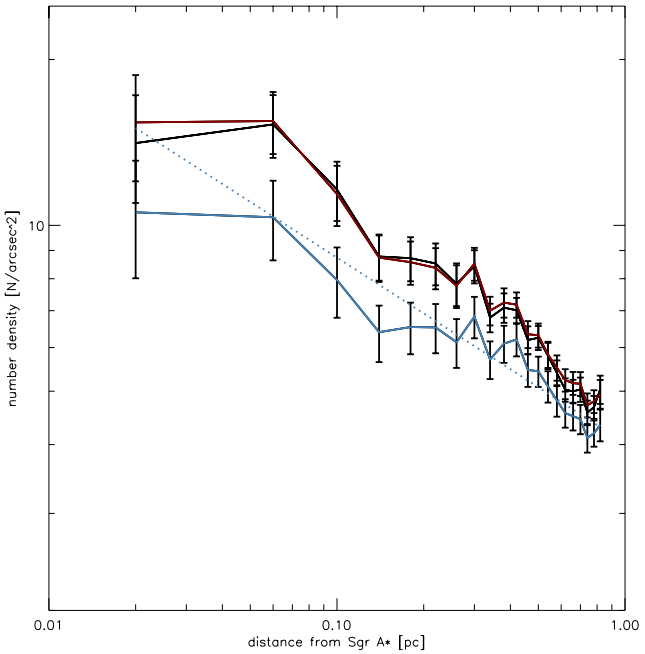

Fig. 11. Mean surface density profile for stars with ($17.5 \leq K_s \leq 18.5$), after averaging over the four runs with different *Starfinder* parameters. Blue: Uncorrected data. Red: Data corrected for crowding. Black: Data corrected for crowding and extinction.

the applied correction factors, albeit necessary, do not significantly alter our results. This shows that our data are robust.

Table 2. Parameters used in the estimation of the surface density profile of pre-MS stars and resulting corrected Γ for the density profile of stars with magnitudes $17.5 \leq K_s \leq 18.5$.

ID	η^a	N^b	Γ^c
1[d]	1.40	146	-0.41± 0.03
2[e]	0.93	200	-0.41± 0.03
3[f]	1.10	200	-0.39± 0.03
4[g]	0.93	300	-0.37± 0.03
5[h]	1.10	300	-0.36± 0.03

Notes.

[a] Power-law index of the surface-density profile.

[b] Total number of pre-MS stars at $R = 0.8" - 12.5"$.

[c] Power-law index of the surface-density profile of faint stars ($17.5 \leq K_s \leq 18.5$) after correction for pre-MS stars,

[d] Value of the η-parameter from (Bartko et al. 2010).

[e] Value of the η-parameter from (Do et al. 2013).

[f,h] Intermediate value of the η-parameter to test.

[g] Value of the η-parameter from (Do et al. 2013).

4.2. Tracer populations

With an approximate magnitude of $K_s = 18$, the faintest stars in our sample are consistent with being (sub-)giants on the ascending branch or main sequence (MS) stars of ~2.5 $M_\odot$. They could also be pre-MS stars of a few solar masses or less (Lu et al. 2013). From what is known about the star formation history of the NSC we expect that the majority of stars is old (~80% of the NSC's mass were formed > 5 Gyr ago, according to Pfuhl et al. 2011) and that most of the faint stars in our sample are thus old, (sub-)giants. However, since we know that a star formation event created on the order 10^4 $M_\odot$ of young stars in the region about 0.5 pc around Sgr A*, contamination by a significant amount of pre-MS objects is possible. We will discuss this possibility in the next subsection.

4.3. Possible contamination by pre-MS stars

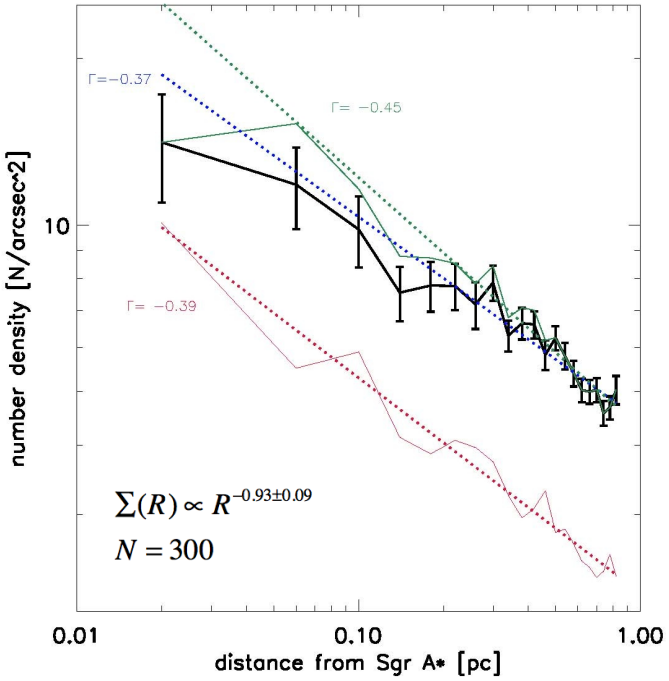

Fig. 12. Measured extinction and crowding-corrected surface number density profiles for $16.5 \leq K_s \leq 17.5$ (red line) and $17.5 \leq K_s \leq 18.5$ (green line). The black line represents the surface density profile for $17.5 \leq K_s \leq 18.5$ after correction for the possible contamination by pre-MS stars, using $\eta = 0.93 \pm 0.09$ (Do et al. 2013) and $N = 300$, roughly estimated by using the information in Fig. 15 of Lu et al. (2013). The dotted lines are simple power-law fits to the data and their corresponding indices are indicated in the panel.

Our primary goal in this study is to determine the spatial distribution of the old, relaxed stellar population at the GC. Care must therefore be taken to exclude young and therefore probably dynamically unrelaxed stars. We have excluded from the analysis all spectroscopically identified early-type stars from Do et al. (2013). Unfortunately, the limit of spectroscopic identification of early-type stars with current instruments is $K_S \approx 16$ in the GC (with the exception of a few, very deep exposures of small fields that reached $K_s \approx 17.5$, see Pfuhl et al. 2011). As argued in the previous section, the star formation event that took place a few Myr ago in the central $R \approx 0.5$ pc means that we have to consider explicitly the possibility that our stellar surface number densities are contaminated by pre-MS stars.

To do this, we assume that the density profile of the young stars can be described by a simple power-law (e.g., Bartko et al.

2010; Lu et al. 2013). The main parameters to take into account are: η, the index of the power law and N, the total number of young stars in the magnitude range $17.5 \leq K_s \leq 18.5$ and within $R \leq 12$". We assumed different values of η and N from the literature, subtracted the resulting pre-MS number density profiles and then derived the power-law indices of the profiles for the corrected number density profiles, as summarised in Table 2. In Fig. 12 we show the surface density profile for stars of $17.5 \leq K_s \leq 18.5$ both with and without correction of contamination by pre-MS stars. As can be seen from the different values in Table 2 , taking the possible bias from pre-MS stars into account with a range of reasonable values, can reduce the measured power-law index from $\Gamma = -0.51 \pm 0.02$ to $\Gamma = -0.36 \pm 0.03$. This value is the most conservative one from our estimates because it assumes the highest contamination rate by pre-MS stars, and we will adopt it here as a measure for the projected surface density of old, faint stars. We note that in Paper II we find $\Gamma_{diffuse} = -0.28 \pm 0.03$ for the surface density of even fainter, unresolved stars. The two values overlap within their $2\,\sigma$ uncertainties.

The value of $\Gamma = -0.36 \pm 0.03$ lies $> 10\,\sigma$ away from a flat core. Finally, we also note that the best power-law fit to the surface number density of stars in the range $16.5 \leq K_s \leq 17.5$ results in a very similar $\Gamma = 0.39 \pm 0.03$. Although there is some uncertainty as to whether stars in this brightness range are suitable tracers of a relaxed population, it is reassuring to note that this value coincides with the pre-MS corrected Γ of the faintest tracers. Since the magnitude range $16.5 \leq K_s \leq 17.5$ would correspond to more massive – and this shorter-lived – pre-MS stars, we expect a weaker pre-MS contamination in this range (see also Fig. 5 in Lu et al. 2013).

4.4. 3D profile: Nuker fit

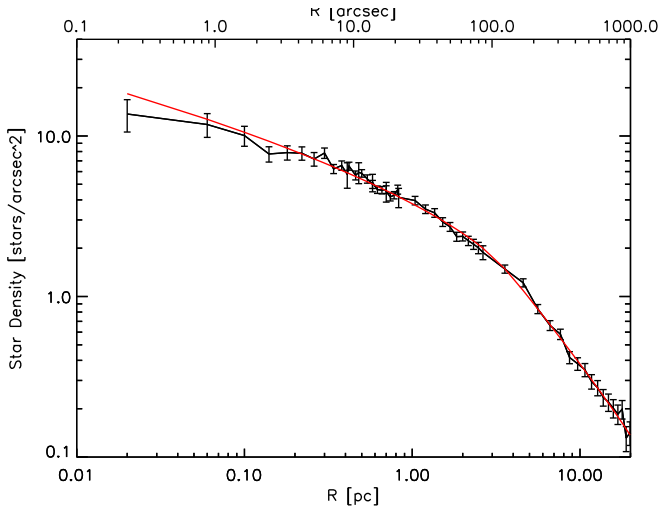

Fig. 13. Nuker model fit (red line) to the surface density profile for $17.5 \leq K_s \leq 18.5$ corrected for the contamination by pre-main sequence stars in the region 0.8"-12.5".

In order to convert the measured 2D profile into a 3D density law, we need to deal with projection effects, which requires us to constrain the surface density on scales larger than what we could measure with NACO. For this purpose we use the data from Fritz et al. (2016), which they acquired from observations with NACO/VLT, WFC3/HST, and VIRCAM/VISTA. To combine these data with ours, we have to assume that, on large scales, the NSC stellar population is well mixed and that its average properties (mass function) do not change. We scaled the data of Fritz et al. (2016) to ours in the range $0.5\,\mathrm{pc} \leq R \leq 0.9\,\mathrm{pc}$ to our surface number density for stars $17.5 \leq K_s \leq 18.5$, corrected for the possible presence of pre-MS stars with the parameters from model ID 4 in Table 2. Subsequently, we subtracted a constant star density offset to take into account the contribution of the stars that do not belong to the nuclear cluster but to other structures, such as the nuclear disk or the Galactic Bulge. This simple procedure is possible because the scale lengths of the latter components are one to several orders of magnitude larger than the half-light radius of the NSC (see, e.g., Launhardt et al. 2002; Bland-Hawthorn & Gerhard 2016).

We used a 3D *Nuker* model (Lauer et al. 1995) as given in equation 1 of Fritz et al. (2016) and projected it onto the sky to fit the surface density profiles at $R \leq 20\,\mathrm{pc}$. The fits were repeated several times, using different values for the subtracted constant star density and for the innermost radial data range that was included in the fit. We also performed a fit without the correction for the potential pre-MS stars. The results of our fits are listed in Table 3. While the parameters r_b (break radius) and β (outer power-law index) vary significantly, γ (inner power-law index) shows consistent values for all fits, which is reassuring because it is the most important parameter for this work, where we are interested in whether there exists of stellar cusp at the GC. Fit IDs 1 and 2 explore extreme values for the subtracted constant star density. We use the mean and error of the mean of the parameters of the other four fits to obtain orientative values for the average best Nuker model: $r_b = 3.0 \pm 0.4$ pc (77 ± 10"), $\gamma = 1.29 \pm 0.02$, $\beta = 2.1 \pm 0.1$, and a density at the break radius of $\rho(r_b) = 3900 \pm 900\,\mathrm{pc}^{-3}$. The best fit according to line 4 in Table 3 is shown in Fig. 13.

The Nuker fit shows that the faint stars show a cusp-like distribution around Sgr A*. A flat core can be excluded with high significance. We explicitly note that in the fits presented in this work we omit the region $R \leq 1$" (0.04 pc). In this region, the star counts appear to drop slightly below the expected levels. However, this region is also the most crowded region, which may lead to strong systematics in the star counts. Additionally, the stellar population in the extremely close environment of Sgr A* may have been altered, as is indicated by the presence of the so called "S-stars", apparently B-type MS stars that appear concentrated within $R < 1$" of Sgr A* and may have been deposited there by individual scatter or capture events (see, e.g., Eisenhauer et al. 2005; Genzel et al. 2010; Alexander 2011).

4.5. Distribution of giant stars near Sgr A*

In agreement with previous work, we have found an unexpectedly flat surface density for RC stars and brighter giants within about 0.3 pc of Sgr A*. This may indicate a possible deficit of giants in this region. Here we produce a 3D Nuker model fit for the giant stars and try to constrain the number of potentially missing giants. We proceeded as in section 4.4. At large radii, we used the data from Fritz et al. (2016) and subtracted a constant density of 0.07 stars per square arcsecond from the data. We produced fits for RC stars, using as a proxy for the selection of RC stars that the RC bump in the K_s LF is comprised approximately between $15 \leq K_s \leq 16$, and for spectroscopically identified giant stars ($K_s \leq 15.5$) for different ranges of R. The resulting best-fit parameters are given in Table 4.

As can be seen from the reduced χ^2 values, the quality of the fit improves as we omit the central most data points. Overall, the surface densities of RC stars and spectroscopically identi-

Table 3. Best-fit model parameters for the Nuker fits.

ID	r_b (pc)	γ	β	$\rho(r_b)$ (mJy pc^{-3})	$\chi^2_{reduced}$
1[a]	1.13 ± 0.28	1.17 ± 0.1	1.63 ± 0.02	0.84 ± 0.31	1.7
2[b]	5.73 ± 0.38	1.36 ± 0.03	3.73 ± 0.23	0.07 ± 0.01	1.1
3[c]	3.80 ± 0.34	1.33 ± 0.03	2.31 ± 0.05	0.14 ± 0.02	0.7
4[d]	3.63 ± 0.32	1.31 ± 0.03	2.30 ± 0.05	0.15 ± 0.02	0.7
5[e]	2.13 ± 0.26	1.23 ± 0.05	1.92 ± 0.3	0.35 ± 0.07	0.8
6[f]	2.44 ± 0.34	1.30 ± 0.04	1.94 ± 0.03	0.28 ± 0.06	0.9

Notes. [(a)] 0.01 stars arcsec^{-2} constant number density subtracted. Fit range $0 \leq R \leq 20$ pc .
[(b)] 0.1 stars arcsec^{-2} constant number density subtracted. Fit range $0 \leq R \leq 20$ pc .
[(c)] 0.07 stars arcsec^{-2} constant number density subtracted. Fit range $0.04 \leq R \leq 20$ pc .
[(d)] 0.07 stars arcsec^{-2} constant number density subtracted. Fit range $0.0 \leq R \leq 20$ pc .
[(e)] 0.05 stars arcsec^{-2} constant number density subtracted. Fit range $0.0 \leq R \leq 20$ pc .
[(f)] 0.05 stars arcsec^{-2} constant number density subtracted. Fit range $0.0 \leq R \leq 20$ pc. No correction for pre-MS stars .

Table 4. Best-fit model parameters for the Nuker fits to the densities of giant/RC stars.

ID	r_b (pc)	γ	β	$\rho(r_b)$ (arcsec^{-3})	$\chi^2_{reduced}$
1[a]	2.0 ± 0.27	1.06 ± 0.06	2.12 ± 0.05	0.21 ± 0.04	2.7
2[b]	3.10 ± 0.45	1.23 ± 0.04	2.25 ± 0.07	0.10 ± 0.02	2.2
3[c]	4.57 ± 0.50	1.45 ± 0.03	2.35 ± 0.06	0.05 ± 0.01	0.7
4[d]	4.28 ± 0.54	1.41 ± 0.04	2.34 ± 0.07	0.05 ± 0.01	1.2
5[e]	3.22 ± 0.50	1.25 ± 0.05	2.27 ± 0.08	0.09 ± 0.02	2.2
6[f]	2.98 ± 0.47	1.22 ± 0.05	2.24 ± 0.08	0.09 ± 0.02	2.7
7[g]	4.22 ± 0.59	1.39 ± 0.04	2.34 ± 0.08	0.05 ± 0.01	1.5

Notes. [(a)] RC stars. Fit range $0 \leq R \leq 20$ pc .
[(b)] RC stars. Fit range $0.04 \leq R \leq 20$ pc .
[(c)] RC stars. Fit range $0.3 \leq R \leq 20$ pc .
[(d)] RC stars. Fit range $0.2 \leq R \leq 20$ pc .
[(e)] RC stars. Fit range $0.1 \leq R \leq 20$ pc .
[(f)] Spectroscopically identified giants. Fit range $0 \leq R \leq 20$ pc .
[(g)] Spectroscopically identified giants. Fit range $0.2 \leq R \leq 20$ pc .

fied giants agree well with a stellar cusp of similar properties as measured for the fainter stars. We use the mean and error of the mean of the parameters of the fits to the RC stars to obtain orientative values for the average best Nuker model for RC stars: $r_b = 3.4 \pm 0.5$ pc (110 ± 13"), $\gamma = 1.28 \pm 0.07$, $\beta = 2.26 \pm 0.04$, and $\rho(r_b) = 1700 \pm 500\,\mathrm{pc}^{-3}$. As we can see, the mean parameters agree very well with the ones determined from the Nuker fits to the faint stars. The best fits according to lines 4 and 7 in Table 4 are shown in Fig. 14.

The observed flat profile within a few 0. pc and the fact that the quality of the fit improves when we omit the innermost data points may indicate that something has altered the apparent distribution of giants in this region. To estimate the number of potentially "missing" giants, we focus on the region $R \leq 0.3$ pc. Since it is impossible to know what would be the "correct" number density model for giants stars, we use the following simple approach. We fit different Nuker laws to the data, where we omit the data inside $R = 0.0, 0.1, 0.2, 0.3$ pc. The fit for $R = 0.0$ is the benchmark for the actually measured distribution, while the fits that omit data approximate the cluster structure without potentially missing stars at small R. The data for spectrosocpically identified bright giants are shown in Fig. 15, along with the benchmark fit (blue) and the fit omitting data at $R < 0.2$ pc (red).

Subsequently, we compute the amount of stars at $r < 0.2$ pc for each model and compare it to the benchmark solution. The difference in number provides the estimate of possibly missing stars at $r < 0.2$ pc. For the three fits that omit data at small R, this numbers varies between 50 to 90. While the uncertainty of this crude estimate is high, it provides us with an idea of the order of magnitude of the problem. The lesson to take away here is, in our opinion, that any mechanisms that intends to explain the deficit of giant stars near Sgr A* should be able to be efficient enough to account for at least a few dozen missing giants.

4.6. Comparison to other work

Consistent with previous work, we find indications of a flattening of the density profile of the RC stars and brighter giants inside $R \approx 8$"/0.3 pc (Buchholz et al. 2009; Bartko et al. 2010; Do et al. 2013). Also, our results agree well with the fits shown for RC stars in Schödel et al. (2007) (their Fig. 17). We also note that the density profile of stars about a magnitude fainter than the RC was analysed in the latter work. Although Schödel et al. (2007) used a broken power-law, it is clear that a single power-law, with $\Gamma \approx 0.4$, would also provide a satisfactory fit to the stars fainter than the RC (see right panel in their Fig. 17). Yusef-Zadeh et al. (2012) determined the surface light density of faint

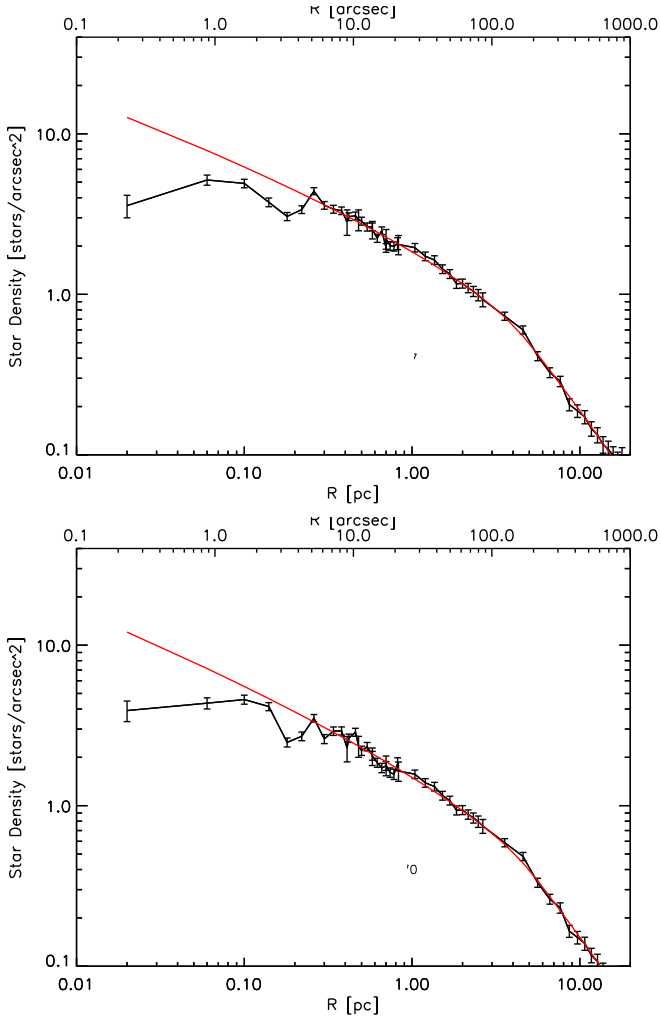

Fig. 14. Nuker model fits (red lines, models 4 and 7 in Tab, 4) to the surface density profile for RC stars (upper panel) and bright ($K_s \leq 15.5$), spectroscopically identified giants (lower panel).

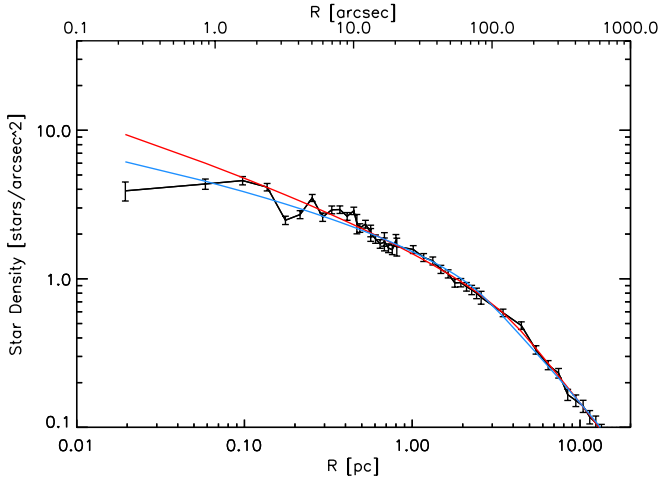

Fig. 15. 2D Nuker model fits to the surface density profile for bright, spectroscopically identified giants. The blue line is a fit that includes the data at $R \leq 0.3$ pc, while the red line omits these data.

stars in HST/NICMOS images at 1.45, 1.70, and 1.90 μm. After the masking of bright sources, the stars that dominate the light profiles presented in Yusef-Zadeh et al. (2012) are probably slightly fainter than the RC and show a single power-law profile with $\Gamma = 0.34 \pm 0.04$ at 5" $\leq R \leq$ 0.7", in agreement with what we find in this work and with the surface density of stars fainter than the RC shown in Schödel et al. (2007). To conclude, our analysis agrees well with previously published results.

There are also several key differences between previous work and our analysis, which goes beyond the existing state-of-the-art:

1. We reach about one magnitude deeper in the KLF and are not limited/dominated by stars in the RC or bright giants.
2. We focus explicitly on well defined brightness ranges to have a constraint on the ages and masses of the stars that we are studying, while most previous work generally reported surface density profiles for broad ranges of luminosities (but was mostly dominated by RC stars).
3. We include high angular resolution data on larger radii, out to $R \approx 2$ pc (the only other work to do so was by Fritz et al. 2016).
4. We include the most recent data on the large-scale structure of the NSC and thus take into account its global structure. Much previous work was focused on the innermost region near Sgr A*, e.g., $R <$ 20" (Buchholz et al. 2009), $R \leq$ 5" (Yusef-Zadeh et al. 2012), or $R \leq$ 4" (Do et al. 2009). While these studies found inconsistencies with the existence of a stellar cusp around Sgr A* (with the exception of Yusef-Zadeh et al. 2012), they not only were dominated by bright stars (see above), but also did not take the global picture into account. A stellar cusp is expected to be well developed inside the radius of influence, r_{infl}, of a massive black hole, which is on the order $r_{infl} = 3$ pc for Sgr A* (Alexander 2005; Merritt 2010; Feldmeier et al. 2014; Chatzopoulos et al. 2015a).

The features of the present work have allowed us to infer a more complete picture of the stellar distribution around Sgr A*. In particular, we could show that the surface density distribution of stars fainter than the RC are inconsistent with a flat, core-like distribution with high significance. After taking the possible (and probable) contamination of the faint star counts by pre-MS stars from the last star formation event into account, we find that the surface density of old, (sub-)giant stars (age estimated from their luminosity) at the GC can be approximated well with a single power-law with a power-law index $\Gamma \leq 0.36 \pm 0.03$. This value is similar to what was found by Yusef-Zadeh et al. (2012). It is, however, derived on far deeper star counts over a field-of-view that is almost ten times larger. In particular the faintness of our best tracer population is uniquely suited to study the distribution of the old, probably dynamically relaxed stars at the GC.

In Paper II we study the diffuse stellar light density – probably arising from stars in the magnitude range $K_s = 19 - 20$. We find that the projected diffuse light density can be described well with a simple power-law with an index $\Gamma_{diffuse} = 0.28 \pm 0.03$, similar to the $\Gamma = 0.36 \pm 0.03$ that we here find for the resolved stars of $K_s \approx 18$, after taking contamination by pre-MS stars into account (see section 4.5). We do not expect the surface density profiles of the stars in these different magnitude ranges to be significantly different because the stellar masses are similar and they will share a common star formation history. The lower Γ found for the unresolved stars supports our choice of adopting a relatively high contamination by pre-MS stars for the faint, resolved stars. Also, the differences between the values of Γ can give us an idea of the real uncertainty of our measurements Γ , given that both methods may be biased by unknown systematic biases. Reassuringly, we estimate that the real uncertainty is still

low, on the order ∼0.05. This allows us to claim that there exists a stellar cusp around the massive black hole Sgr A*. A flat core can be rejected with very high confidence.

For the Nuker fits of the 3D density, we find also similar values between the $K_s \approx 18$ stellar population and the fainter, unresolved one studied in Paper II. For the former, we find an inner 3D power-law index of $\gamma_{resolved} = 1.29 \pm 0.02$, for the latter we find $\gamma_{unresolved} = 1.16 \pm 0.02$. Again, we suppose that unknown systemic effects may cause this discrepancy and suggest that the mean of these two values may represent a more realistic, common value for both populations: $\gamma = 1.23 \pm 0.05$. Surprisingly, we find rather different values for β, the power-law index at distances significantly larger than the break radius: $\beta_{resolved} = 2.1 \pm 0.1$ and $\beta_{unresolved} = 3.3 \pm 0.4$. This may indicate that the star counts or diffuse light density suffer from systematic biases at distances $R \gtrsim 2$ pc. We suspect that the diffuse light density may be the less reliable measurement (see additional discussion in Paper II). Reassuringly, the values for the break radius agree within their uncertainties: $r_{b,resolved} = 3.0 \pm 0.4$ and $r_{b,unresolved} = 3.3 \pm 0.3$. We note that the values for r_b derived here are significantly different from what was estimated by Fritz et al. (2016). This is because the surface density in the latter work was dominated by giants/RC stars in the innermost regions. Also, Fritz et al. (2016) fit the surface density of all stars in the GC field (including those from the Galactic Bar and nuclear disk), while we subtracted a constant offset to only take stars in the NSC into account. We point out that the Nuker laws presented here are optimised to describe the intrinsic properties of the nuclear cluster, but *not* the overall stellar density at the GC. The NSC lies, of course, embedded in the overall surrounding structures (e.g., nuclear disc, Galactic Bar/Bulge). The work of Fritz et al. (2016) or Schödel et al. (2014a) provides data that include the large scale stellar structures.

5. Conclusions

In this work we have revisited the question of the distribution of stars around the massive black hole at the centre of the Milky Way because previous studies had come up with the unexpected result that there did perhaps not exist any stellar cusp. To overcome existing limitations, we used improved analysis techniques and deep, stacked images. We could push the completeness limit of star counts about one magnitude deeper than what had been done before, to $K_s \approx 18$. This has allowed us to study a stellar population that consists probably primarily of several Gyr old, $1 - 2\,M_\odot$ stars.

Contrary to the flattening of the density distribution of giant stars near Sgr A*, a well known observation that we also reproduced here, the projected surface density profile of the $K_s \approx 18$ stars can be described very well by a single power-law. After taking the probable contamination of the star counts at $R < 0.5$ pc by pre-MS stars into account, we estimate a power-law index of $\Gamma = -0.36 \pm 0.05$. The cited uncertainty of this value is somewhat larger than what we derived formally in section 4.3 because it takes into account the comparison with the power-law index for the unresolved stellar population that we determined in Paper II. Both the $K_s \approx 18$ resolved stars and the even fainter, unresolved stars studied in Paper II show consistent projected surface densities around Sgr A*. We can thus exclude a core-like stellar density distribution with high confidence and claim the existence of a stellar cusp of old, dynamically relaxed stars around Sgr A*.

We fit 3D Nuker models to the data to estimate the intrinsic structure of the Milky Way's NSC. From our comparison between our results from this work and from Paper II, we estimate that the stellar cusp has a 3D power-law index of $\gamma = 1.23 \pm 0.05$. The break radius of the Nuker model lies at about 3 pc, which corresponds to the radius of influence of Sgr A*. This agrees with theoretical expectations that the cusp is visible well inside the break radius (e.g., Alexander 2005).

The stellar cusp around Sgr A* appears to be significantly flatter than the theoretically expected value of $\gamma_{theor} = -1.5$ for the low-mass stellar component in a multi-mass cluster (see Alexander 2005, and references therein). Some disagreement with theory is to be expected, however. After all, the Milky Way's NSC is more complex than what was considered in existing theoretical work. For example, it is embedded in a complex environment, has a complex star formation history, and may have suffered events of infall and accretion of smaller clusters (e.g., Pfuhl et al. 2011; Feldmeier et al. 2014; Schödel et al. 2014b). New N-body simulations, that were undertaken in parallel to this observational work (Paper III, Baumgardt, Amaro-Seoane & Schödel, submitted to A&A) and that included the effect of repeated star formation events, find flat cusp slopes in agreement with our findings.

Finally, the existence of a stellar cusp may implies that the giant stars around Sgr A* do indeed display a deficiency in numbers within a projected radius of a few 0.1 pc. We estimate that a few dozen giants may be "missing". This region overlaps with the region where we find young massive stars that may have formed in a dense gas disc a few Myr ago. Repeated collisions with proto-stellar clumps in this disc may have stripped the giants of their envelopes, rendering them thus unobservable (Amaro-Seoane & Chen 2014; Kieffer & Bogdanović 2016).

Acknowledgements. The research leading to these results has received funding from the European Research Council under the European Union's Seventh Framework Programme (FP7/2007-2013) / ERC grant agreement n° [614922]. PAS acknowledges support from the Ramón y Cajal Programme of the Ministry of Education and Science of Spain. This work is based on observations made with ESO Telescopes at the La Silla Paranal Observatory under programmes IDs 183.B-0100 and 089.B-0162.

References

Aharon, D. & Perets, H. B. 2015, ApJ, 799, 185
Alexander, T. 2005, Phys. Rep., 419, 65
Alexander, T. 2011, in Astronomical Society of the Pacific Conference Series, Vol. 439, The Galactic Center: a Window to the Nuclear Environment of Disk Galaxies, ed. M. R. Morris, Q. D. Wang, & F. Yuan, 129
Alexander, T. & Hopman, C. 2009, ApJ, 697, 1861
Amaro-Seoane, P. & Chen, X. 2014, ApJ, 781, L18
Amaro-Seoane, P., Freitag, M., & Spurzem, R. 2004, MNRAS, 352, 655
Bahcall, J. N. & Wolf, R. A. 1976, ApJ, 209, 214
Bartko, H., Martins, F., Trippe, S., et al. 2010, ApJ, 708, 834
Baumgardt, H., Makino, J., & Ebisuzaki, T. 2004, ApJ, 613, 1143
Bland-Hawthorn, J. & Gerhard, O. 2016, ARA&A, 54, 529
Boehle, A., Ghez, A. M., Schödel, R., et al. 2016, ApJ, 830, 17
Böker, T. 2010, in IAU Symposium, Vol. 266, IAU Symposium, ed. R. de Grijs & J. R. D. Lépine, 58–63
Buchholz, R. M., Schödel, R., & Eckart, A. 2009, A&A, 499, 483
Chatzopoulos, S., Fritz, T. K., Gerhard, O., et al. 2015a, MNRAS, 447, 948
Chatzopoulos, S., Gerhard, O., Fritz, T. K., et al. 2015b, MNRAS, 453, 939
Dale, J. E., Davies, M. B., Church, R. P., & Freitag, M. 2009, MNRAS, 393, 1016
Diolaiti, E., Bendinelli, O., Bonaccini, D., et al. 2000, A&AS, 147, 335
Do, T., Ghez, A. M., Morris, M. R., et al. 2009, ApJ, 703, 1323
Do, T., Kerzendorf, W., Winsor, N., et al. 2015, ApJ, 809, 143
Do, T., Lu, J. R., Ghez, A. M., et al. 2013, ApJ, 764, 154
Eisenhauer, F., Genzel, R., Alexander, T., et al. 2005, ApJ, 628, 246
Feldmeier, A., Neumayer, N., Seth, A., et al. 2014, A&A, 570, A2
Fritz, T. K., Chatzopoulos, S., Gerhard, O., et al. 2016, ApJ, 821, 44
Fritz, T. K., Gillessen, S., Dodds-Eden, K., et al. 2011, ApJ, 737, 73
Genzel, R., Eisenhauer, F., & Gillessen, S. 2010, Reviews of Modern Physics, 82, 3121
Genzel, R., Schödel, R., Ott, T., et al. 2003, ApJ, 594, 812

Gillessen, S., Plewa, P., Eisenhauer, F., et al. 2016, ArXiv e-prints [arXiv:1611.09144]
Gültekin, K., Richstone, D. O., Gebhardt, K., et al. 2009, ApJ, 698, 198
Kieffer, T. F. & Bogdanović, T. 2016, ApJ, 823, 155
Knuth, K. H. 2006, ArXiv Physics e-prints [arXiv:physics/0605197]
Lauer, T. R., Ajhar, E. A., Byun, Y.-I., et al. 1995, AJ, 110, 2622
Launhardt, R., Zylka, R., & Mezger, P. G. 2002, A&A, 384, 112
Lightman, A. P. & Shapiro, S. L. 1977, ApJ, 211, 244
Löckmann, U., Baumgardt, H., & Kroupa, P. 2010, MNRAS, 402, 519
Lu, J. R., Do, T., Ghez, A. M., et al. 2013, ApJ, 764, 155
Merritt, D. 2010, ApJ, 718, 739
Meyer, L., Ghez, A. M., Schödel, R., et al. 2012, Science, 338, 84
Murphy, B. W., Cohn, H. N., & Durisen, R. H. 1991, ApJ, 370, 60
Nishiyama, S., Tamura, M., Hatano, H., et al. 2009, ApJ, 696, 1407
Pfuhl, O., Fritz, T. K., Zilka, M., et al. 2011, ApJ, 741, 108
Preto, M. & Amaro-Seoane, P. 2010, ApJ, 708, L42
Schödel, R. 2010, A&A, 509, A260000+
Schödel, R., Eckart, A., Alexander, T., et al. 2007, A&A, 469, 125
Schödel, R., Feldmeier, A., Kunneriath, D., et al. 2014a, A&A, 566, A47
Schödel, R., Feldmeier, A., Neumayer, N., Meyer, L., & Yelda, S. 2014b, Classical and Quantum Gravity, 31, 244007
Schödel, R., Merritt, D., & Eckart, A. 2009, A&A, 502, 91
Schödel, R., Najarro, F., Muzic, K., & Eckart, A. 2010, A&A, 511, A18+
Schödel, R., Yelda, S., Ghez, A., et al. 2013, MNRAS, 429, 1367
Trippe, S., Gillessen, S., Gerhard, O. E., et al. 2008, A&A, 492, 419
Witzel, G., Eckart, A., Bremer, M., et al. 2012, ApJS, 203, 18
Yusef-Zadeh, F., Bushouse, H., & Wardle, M. 2012, ApJ, 744, 24